Simultaneous measurement of thermal conductivity and interfacial thermal resistance of Sub-10 nm SWCNT bundle via Raman-probing of distinct energy transport states

Ibrahim Al Keyyam [a], Baini Li [b], Tianyu Wang [b,**], Cheng Deng [c,***], Xinwei Wang [a,*]

[a] *Department of Mechanical Engineering, Iowa State University, Ames, IA, 50011, USA*
[b] *Research Center for Industries of the Future, Key Laboratory of 3D Micro/Nano Fabrication and Characterization of Zhejiang Province, School of Engineering, Westlake University, Hangzhou, 310024, PR China*
[c] *College of Mechatronics Engineering, Guangdong Polytechnic Normal University, Guangzhou, 510635, PR China*

ABSTRACT

Recent studies have shown that the thermal conductivity (κ) of single-walled carbon nanotubes (SWCNTs) can dramatically change due to structural changes within the same sample. This introduces substantial uncertainty to interfacial thermal resistance (ITR) measurement, which usually relies on pre-measured κ. Herein, we implement a novel transient Raman technique to distinguish and simultaneously measure the κ and ITR of a SWCNT bundle of less than 10 nm by employing multiple laser heating sizes, each carrying distinct information about the ITR and κ. The ITR is measured as 975–1200 K m W^{-1} whereas κ is 180–246 W m^{-1} K^{-1}. The ITR shows a decreasing trend against increased bundle size, demonstrating the impact of contact area in local energy transport. The measured κ is approximately 33 % of supported graphene reported in literatures. This significant κ reduction is attributed to the structural defects in the sample and the bundling effect consistent with earlier studies.

1. Introduction

Due to their exceptional mechanical and thermophysical properties, carbon nanotubes (CNTs) have attracted significant interests in various applications [1]. The thermal conductivity (κ) of CNTs has been intensively investigated in the past, and the reported values for κ span a vast range of 10–5000 W m^{-1} K^{-1}, some of which are summarized in Table 1. In a recent study by Feng et al. [2], it was demonstrated that the κ could decrease by 75 % for the same single-walled CNT (SWCNT) sample due to structural changes. An earlier study by Feng et al. investigated the impact of the bundle size of SWCNTs and its impact on κ when compared to individual SWCNTs [3]. The results show that the κ of a SWCNT bundle with 13 SWCNTs can be two orders of magnitude lower than that of individual SWCNTs. The results can be explained by the tube-tube interactions, which give rise to an internal interfacial thermal resistance (ITR) within the bundle and the presence of interstitial spaces. A recent work by Shiga et al. [4] confirmed the impact of bundling on phonon transport in SWCNTs. The results suggest that the impact is magnified at length scales of SWCNT bundles greater than 1 μm and is even more prominent at low temperatures, consistent with previous findings in literature [5]. Furthermore, it has been found that thermal transport in SWCNT bundles depends on the curvature and configuration within the bundle, even for the same number of individual SWCNTs. The reduction in κ due to tube interactions has also been observed in multi-walled CNTs (MWCNTs) which lowers their in-plane κ [6,7], which is also the basis for the lower κ of vertically aligned carbon nanotubes [8].

During ITR measurements, the determination of ITR requires knowledge of κ, which usually takes pre-measured values. Therefore, unknown variation in reported κ influences the inferred ITR between CNTs and different substrates, even for the same substrate. Yang et al. studied the contact transition from cross-contact to aligned contact on the ITR between MWCNTs and observed two orders of magnitude reduction when the contact is aligned. The reported results were in the order of 10^{-7}-10^{-9} K m^2 W^{-1} [9]. Maune et al. observed an ITR of about 3 K m W^{-1} between a SWCNT and sapphire substrate [10]. Their

---

Table 1
Summary of reported room-temperature κ of CNTs.

	Method	Length (μm)	Diameter (nm)	κ (W·m^{-1} K^{-1})
SWCNT [15]	Optothermal Raman	10	1.88	1439–2317
SWCNT [15]	Optothermal Raman	5	2	720
SWCNT [2]	Optothermal Raman	5.2	3	700–900
SWCNT [13]	FET-Raman	>10	6.7	50
SWCNT [3]	Joule Heating	–	–	200–5000
MWCNT [16]	3ω	1.4	20	300
SWCNT [17]	Molecular dynamics	5–40	3.47–3.68	10–375
SWCNT [4]	Molecular dynamics	0.005–10	–	1000–2000

research highlights that efficient thermal transport requires an adequate contact length between the SWCNT and substrate, with the dominant limiting factor being the interfacial resistance rather than the conduction resistance within the substrate itself. Shi et al. [11] probed a 1.2 nm-thick metallic SWCNT on a SiO$_2$ substrate using a Joule heating approach. Their findings revealed that the ITR at room temperature ranged from 17 to 142 K m W^{-1}. The method they employed to determine the ITR notably depends on the κ values for the SWCNT, which were assumed to be within a range of 1000–3000 W m^{-1} K^{-1}. Al Keyyam et al. [12] investigated the ITR at the SWCNT/Si interface and found it to be $(1.67–3) \times 10^3$ K m W^{-1}. The κ used in the work was 50 W m^{-1} K^{-1} based on another study done earlier by the same group for suspended SWCNT bundle [13].

The uncertainty in κ in the previous two studies significantly impacts the inferred ITR by an order of magnitude. Furthermore, as mentioned earlier, κ can change drastically from location to location within the same sample [2]. Hence, developing a technique that simultaneously measures κ and ITR for the exact location is particularly interesting and important. Several experimental techniques have been adopted in literature to characterize the thermophysical properties of 1D and 2D materials. Nano-resolved Raman measurement offers an excellent advantage for its non-contact nature and high resolution. A detailed summary of different Raman techniques can be found in our recent work [14].

Here, using the Frequency-domain Energy Transport state-resolved Raman (FET-Raman), we develop a technique to characterize the thermal transport in the in-plane and cross-plane directions for the SWCNT/SiO$_2$ interface. The main advantage of the FET-Raman is that it eliminates uncertainties associated with laser absorption measurements and Raman temperature calibration, which are associated with conventional Raman thermometry probing. The technique used in this work proves to be very reliable for simultaneously measuring the κ and ITR of SWCNT bundles of less than 10 nm diameter.

2. Materials and methods

### 2.1. SWCNT synthesis and characterization

SWCNTs are synthesized using the atmospheric pressure chemical vapor deposition (APCVD) technique with sulfur, ferrocene, and xylene as precursors. A nickel foil is placed downstream within a quartz tube inside the CVD furnace. The furnace temperature is increased to 1160 °C under an argon gas flow. A precursor solution of sulfur and ferrocene dissolved in xylene is then introduced upstream in the quartz tube, accompanied by a change in the carrier gas to an argon-hydrogen mixture. The gas flow rates are precisely controlled to optimize the growth conditions. The reaction duration is varied to regulate the

thickness of the synthesized SWCNT layers. Aligned SWCNT arrays are fabricated by transferring the SWCNT film onto a 300 nm SiO$_2$ layer on Si. A nylon filter moistened with ethanol is wrapped around a razor blade to provide a cushioning layer, ensuring uniform force distribution. The razor blade is then pressed against the SWCNT network film and moved unidirectionally over the substrate, aligning the SWCNTs in the direction of motion [18].

In this study, four distinct locations (designated numerically 1 through 4) of the same SWCNT bundle are probed and characterized to determine their ITR and κ. This is crucial to assess the feasibility of our technique and uncover how these properties might vary from location to location within the same sample. Atomic force microscopy (AFM) is used to study the sample profile. Fig. 1a shows a 3D scan for Location #2 of the sample, which is highlighted, and its height is measured in Fig. 1b. The green shaded area represents the laser spot location in the Raman measurement. The sample height at Location #2 is shown to be around 8 nm with a variation from 6 to 10 nm along the bundle's length direction, as shown in Fig. 1c. However, the laser spot size in the Raman measurement covers a larger area than the localized AFM measurement shown in Fig. 1a. We observe that the bundle's size decreases along its length direction which we believe to have been caused by the aligning process described earlier. This trend has also been observed across the distinct locations studied in Section 3. In our κ and ITR measurement, great measures have been taken to ensure the sample is located at the laser spot center, ensuring the SWCNT bundle receives well-defined laser irradiation. This will ensure the strongest Raman signal and a well-defined laser covering area over the bundle. Prior to collecting the Raman spectra for κ and ITR measurement, we perform a Raman scan in the lateral direction across the bundle to identify the location that gives the highest Raman signal, as illustrated in the schematic in Fig. 1d. When the intensity of the G band is maximized as shown in Fig. 1e, we move on to the next step and perform the Raman analysis as will be described in the following section. The spatial resolution of our positioning stage is 1 nm, which is controlled through piezoelectric actuators and exhibits high stability throughout the experiment. Practically speaking, the center of the bundle could be at the center of the Gaussian laser beam with ±1 nm uncertainty due to the finite resolution of the stage. However, given that the bundle size is orders of magnitude smaller than the beam size, the incident laser energy would not change much within this range. One can show mathematically that the beam's intensity, within 40 nm of the laser beam center of 0.4 μm radius, is about 0.99 of its maximum value. Thus, the sample within ±40 nm of the laser spot center is ensured to receive the maximum laser energy.

2.2. Experimental procedure and underlying physics

The FET-Raman technique used in this work incorporates three distinct energy transport states as follows: a continuous wave (CW) laser under 20× and 100× objectives and a square wave amplitude-modulated laser under 100×. In each energy transport state, the incident laser (532 nm wavelength) induces heating and facilitates Raman scattering. Utilizing different objective lenses (20× and 100×), we effectively vary the heating size, allowing us to distinguish the impact of κ and ITR. To explain the physics behind this, consider an extreme situation where a large laser heating spot fully encompasses the sample. Under these conditions, the in-plane κ of the sample exerts minimal influence on thermal transport in the SWCNT bundle. Hence, the heat conduction is predominantly mediated by the interfacial thermal conductance with the substrate in the cross-plane direction. On the other hand, for a point-like laser source to heat the SWCNT bundle, the role of in-plane κ in thermal transport becomes more prominent. Hence, under the 20× objective lens, the measured thermal response is therefore more sensitive to the ITR, whereas the 100× case is more sensitive to κ of the sample. This method would fail if the sample is entirely encapsulated within the bound of the laser spot area for different objective lenses. However, since the sample's physical length as well as the thermal
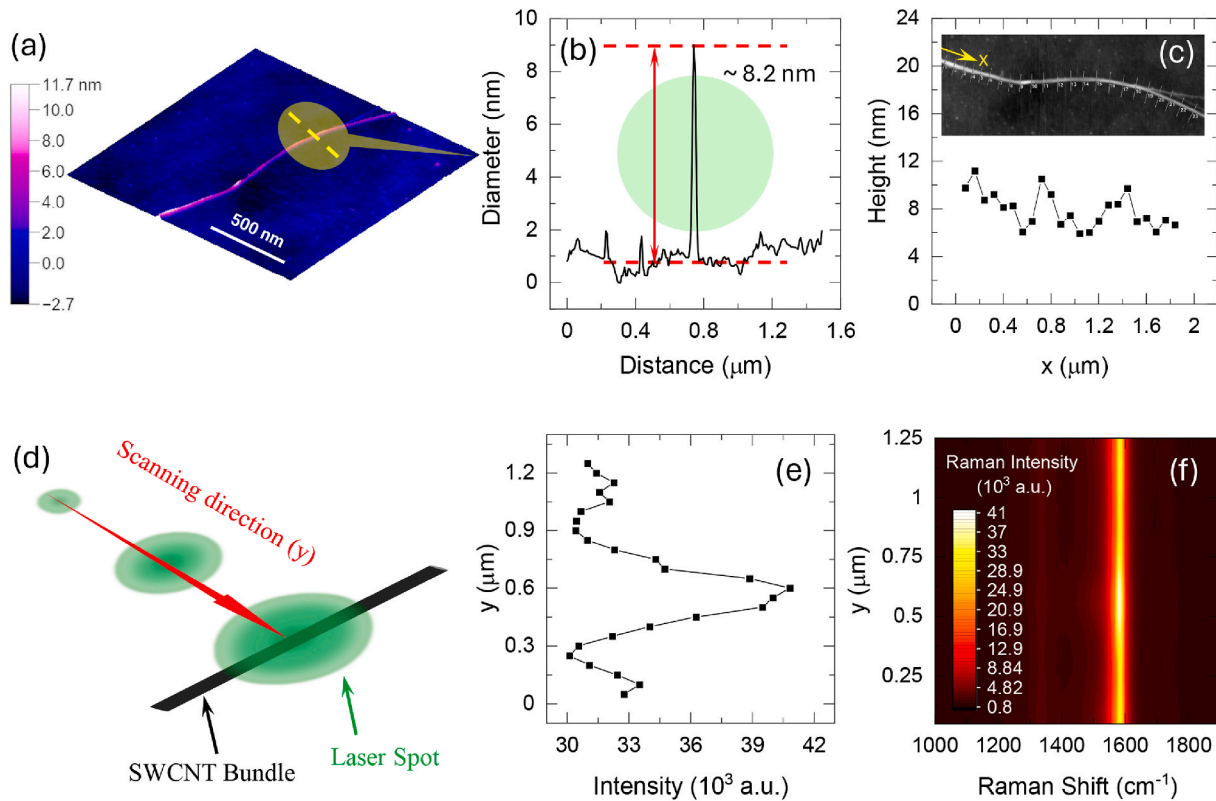
Fig. 1. (a) AFM 3D side view for Location #2 of the SWCNT bundle under study. (b) Precise height measurement with the laser spot size is shown in the green shaded area for Location #2. (c) The AFM height measurements at different locations along the bundle's length direction are shown in the inset. (d) Schematic of the Raman scanning process perpendicular to the axis of the SWCNT bundle. (e) Raman intensity of the G band as a function of laser spot position for the Raman scanning. (f) The 2D contour of the Raman intensity along the scanning position. (For interpretation of the references to colour in this figure legend, the reader is referred to the Web version of this article.)

diffusion length extend beyond the laser spot area, the contribution of axial heat conduction governed by the sample's κ shall be different under different laser spot sizes.

The Raman temperature coefficient determination significantly influences conventional steady-state Raman spectroscopy for thermal characterization, which introduces inherent uncertainties in the results. Additionally, not all the incident laser energy contributes to heating. Determination of laser absorption coefficient most time suffers very large uncertainties. A modulated-laser third-state approach is developed to overcome these limitations, effectively eliminating the dependence on both the laser absorption and Raman temperature coefficients. Each cycle of this modulated laser consists of a laser-on period (t_h) and a laser-off period (t_r), equal in duration and set to 200 ns. The laser pulse duration is chosen after running a series of preliminary tests with different pulse durations to optimize the Raman signal strength and measurement sensitivity. A general rule of t_h selection is that the heat transfer will not reach steady state during this time and the temperature rise during this time is not negligible compared to the quasi-steady state temperature rise. Further details will be given on combining these transient and steady-state measurement results to eliminate the use of laser absorption and knowledge of sample temperature rise.

For each distinct energy transport state, measurements are conducted by varying the laser power (P) using a LabVIEW-controlled automated neutral-density filter to facilitate the experimental procedure. The laser power range is selected to achieve a clear Raman signal and detectable redshift, as shown in Fig. 3d while preventing damage to the sample [19]. Raman spectra are acquired at each laser power using a HORIBA-iHR550 spectrometer. Due to its superior signal-to-noise ratio, the G band ($\sim$1586 cm^{-1}) is used to probe the temperature rise. A Gaussian fitting is applied to pinpoint the G band wavenumber (ω)

within the Raman spectrum. Then, we plot the ω change with P to calculate the Raman shift power coefficient (RSC) denoted as $\psi_{CW} = \partial\omega/\partial P$. This RSC is proportional to the average temperature rise in the sample per 1 mW incident laser power under the laser heating area. The process is repeated under the 100$\times$ and 20$\times$ objectives. The results for location 2 are 0.433 ± 0.03 and 0.0654 ± 0.006 as shown in Fig. 3a and c, respectively. Each ψ_{CW} carries unique information about the contribution of κ and the ITR as discussed earlier. Notably, the average temperature rise which is proportional to ψ is higher under the 100$\times$ than the 20$\times$ due to the larger power density for a smaller laser spot size as shown in Fig. 2. The results for the experimental RSC are summarized in Table 2. A similar procedure is repeated under transient-state heating conditions to determine the RSC (ψ_{FR}). The experimental normalized RSC (Θ_{exp}) is then calculated as $\Theta_{exp} = \psi_{FR}/\psi_{CW}$, which eliminates the necessity for laser absorption and Raman temperature coefficients since Θ_{exp} is solely determined by the thermophysical properties of the SWCNT bundle and its interaction with the substrate. The resolution of the Raman spectrometer lies within 0.5–1 cm^{-1}, for 2400-1200 grating, respectively. The heating/probing is done using the 1200 grating. We note that for FET-Raman, the resolution is more determined by the fitting algorithm accuracy, which can exceed the spectrometer limit to resolve peaks. The slight Raman shift reflects the low temperature rise that prevents heating damage to the sample. The temperature rise in the sample is calculated to be around 32–59 K, which ensures the sample's safety. It has been established earlier that $\Delta\omega$ around 0.6–0.8 cm^{-1} corresponds to the safest operable range for ET-Raman measurements [19].

For any given location, the reported results are obtained after performing the Raman measurement multiple times to optimize the laser focus and ensure minimal uncertainty in RSC. This is important since it
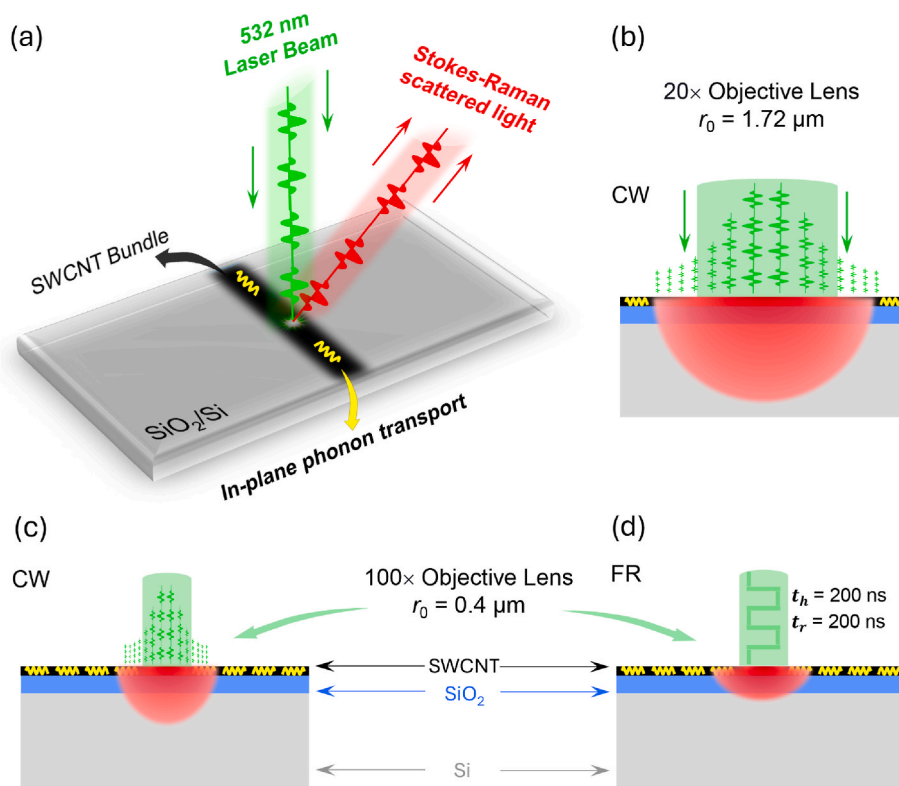
Fig. 2. (a) Schematic of the experimental setup: a 532 nm laser directed towards the supported SWCNT on a SiO_2/Si substrate. The steady-state response using a continuous-wave (CW) laser under (b) 20× and (c) 100× . (d) The transient response under 100× with the heating/relaxation times is set to be 200 ns (2.5 MHz square wave modulation). The red shaded areas represent the heat diffusion areas during laser heating (not to scale, for relative contrast only). (For interpretation of the references to colour in this figure legend, the reader is referred to the Web version of this article.)
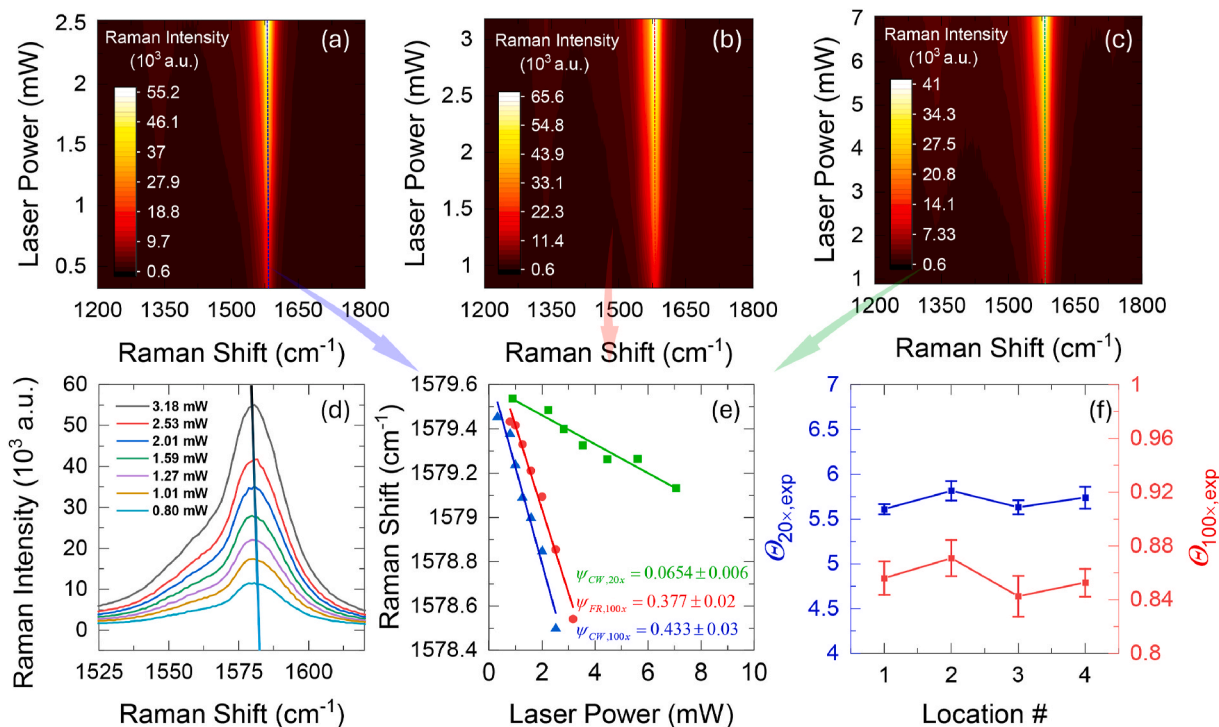
Fig. 3. 2D contour for Raman intensity with different laser powers at Location #2 for (a) CW laser heating under 100× objective lens, (b) amplitude-modulated laser under 100× objective lens, (c) CW laser under 20× objective lens. (d) The G band frequency change (redshift) with incident laser power under 100× . (e) The Raman shift power coefficient (ψ) under different heating scenarios is measured in the unit of $cm^{-1}\ mW^{-1}$. (f) Normalized Raman shift power coefficient (RSC) $\Theta_{exp} = \psi_{FR}/\psi_{CW}$ for different heating scenarios under 20× and 100× objective lens.

Table 2
Summary of the Raman shift power coefficient (ψ) measured in the unit of $cm^{-1}\,mW^{-1}$ for different heating scenarios, the number of distinct RBM peaks, the solid area, and the average individual SWCNT diameter within the bundle ($\widetilde{d}$) for different locations.

Location #	$|\psi_{CW,20\times}|$	$|\psi_{CW,100\times}|$	$|\psi_{FR}|$	# of distinct RBM peaks	Solid Area (nm^2)	$\widetilde{d}$ (nm)
1	0.0602 ± 0.003	0.394 ± 0.03	0.337 ± 0.01	14	16.9	1.48
2	0.0654 ± 0.006	0.433 ± 0.03	0.377 ± 0.02	15	18.6	1.51
3	0.0681 ± 0.004	0.455 ± 0.04	0.382 ± 0.02	15	19.5	1.57
4	0.0474 ± 0.005	0.319 ± 0.01	0.272 ± 0.01	18	21.4	1.46

contributes to the overall uncertainty, so its uncertainty must be minimized. While monitoring the G band, no notable change to its intensity or line shape has been observed, nor have any peaks emerged in the Raman spectrum. This suggests safe operating conditions without sample damage. In our work, the small redshift observed in the G band, which quantifies the temperature rise, is kept minimal to avoid any potential damage to the sample. The estimated temperature rise is around 32–59 K considering Raman temperature coefficients of 0.031 [13] and 0.017 [20]. This is far below other temperature rises recorded in the literature for Raman measurements, which take values between 140 and 600 K [2].

3. Theoretical model development for heat conduction

The theoretical model assumes that the thermal transport is dominated by conduction from the sample to the substrate, where the impact of convection and radiation is negligible. This is confirmed by the 3-5 orders of magnitude lower heat transfer coefficients for convection and radiation when compared to the interfacial energy transport. The convection heat transfer coefficient for air with low Reynold numbers is of the order $\sim$25 W m^{-2} K^{-1}. For a temperature rise of 40 K, the radiation heat transfer coefficient can be calculated as $h_r = \sigma(T_2{}^2 + T_1{}^2)(T_2 + T_1)$, where σ the Stefan-Boltzmann constant, T_1 is the substrate temperature (room temperature), and $T_2 = T_1 + \Delta T$. h_r is determined to be 7.1 W m^{-2} K^{-1}, which justifies its small effect. The uncertainty associated with such assumptions is very minute given the large order of magnitudes when compared to the thermal conductance at the interface as measured in this study as 10^5–10^6 W m^{-2} K^{-1} for a 1–3 nm contact width with the substrate [12].

This study also marks a significant advance in thermal characterization techniques as we simultaneously measure the ITR and κ, where usually one or the other is either dismissed or assumed a pre-measured value. For instance, to measure κ for suspended samples, researchers often dismiss the impact of ITR at the two ends of the sample [2]. Our recent work shows this has a non-negligible impact on the inferred κ for suspended SWCNTs [13]. On the other hand, we, among many other groups, have reported the ITR for supported samples earlier while using a pre-assigned value for κ. The uncertainty of such treatment will be discussed in Section 4.1.

The heat conduction equation(s) for steady and transient states can then be written as:

$$\kappa \frac{\partial^2 T}{\partial x^2} - \frac{T - T_s}{R' \cdot A_c} + \dot{q} = \rho c \frac{\partial T}{\partial t} \tag{1}$$

For steady-state conditions, the transient term on the right-hand side is set to zero. Here, κ denotes the thermal conductivity of the sample and R' is the ITR, both of which are to be determined, ρ is the density, c the specific heat capacity, T_s is the temperature of the substrate, which is assumed to be constant as will be elaborated on shortly, and A_c is the solid cross-sectional area of the SWCNT bundle which will be uncovered via the radial breathing modes (RBM) as will be discussed later in this section.

The thermal response of the three heating scenarios is shown in the schematic diagram in Fig. 2. The red shaded area represents the distance over which heat diffuses through the material within a specific time interval and is characterized by the thermal diffusion length (L_T). For steady-state heating, L_T takes the finite sample size. Since the SiO$_2$ layer dominates the heat conduction resistance within the substrate due to its two orders of magnitude lower κ than silicon, a good approximation for the thermal diffusion length contributing to the thermal conduction resistance is the thickness of the SiO$_2$ layer (300 nm). This calculation is only meant to estimate the thermal conduction resistance of the substrate and does not impact the measurement results. It justifies the assumption that the ITR mainly governs the thermal transport, which was established earlier in the literature [11]. For a transient state, however, the diffusion length has a finite value that depends on the laser heating time (t_e) and the material's thermal diffusivity (α), and is calculated as $L_T = 2\sqrt{\alpha t_e}$. The value is evaluated to be within 575–650 nm for the SiO$_2$/Si substrate. The conduction resistance in the substrate is then calculated $R' = Ln(r_2/r_1)/(2\pi\kappa_s)$ where κ_s is the substrate κ taken as 1.2 W m^{-1} K^{-1} [21], r_1 is the contact width of the sample with substrate and is taken to be 1 nm for order estimation, and r_2 is taken to be the thickness of the SiO$_2$ layer (i.e., 300 nm). The choice of 1 nm is meant to estimate the order of magnitude of the substrate conduction resistance and does not impact the measurements. The value for the contact width (r_1) could be larger than 1 nm, which will further suppress the effect of substrate thermal conduction resistance and justify its negligible contribution in the heat conduction model. By using the thickness of the SiO$_2$ layer for the calculations, we effectively neglect any thermal resistance that might arise in the silicon wafer. This is justified since κ of Si is roughly 100 times that of SiO$_2$. By substituting the values, we calculate the induced substrate thermal resistance during the laser heating, dominated by the SiO$_2$ layer, as 0.65 K·m·W^{-1}. This substrate conduction resistance is about three orders of magnitude lower than the ITR measured previously to be between 530 and 725 K m W^{-1} for the SWCNT/SiO$_2$ interface at room temperature [20]. Thus, we validate our assumption of a negligible temperature rise in the substrate. We also assume that heat transfer in the thickness direction is predominantly governed by the ITR, where the conduction resistance across the thickness of the bundle is negligible, as shown in multiple studies done earlier on supported low-dimensional materials [22–24].

The induced laser heating ($\dot{q}$) is represented by a Gaussian profile and is defined as:

$$\dot{q}(x) = \dot{q}_0 \exp(-x^2/r_0^2), \tag{2}$$

where $\dot{q}_0$ is the peak heat source at the center of the laser beam ($x = 0$), and r_0 is the radius of the laser beam, which has been measured to be 0.4 and 1.76 µm for 100$\times$ and 20$\times$ objectives at the e^{-1} peak intensity, as illustrated in Fig. 2. The heat conduction equation is then solved numerically using the finite volume method to obtain the temperature rise in the sample under the laser heating as a function of the ITR and κ. This is done for the three scenarios: steady-state heating under 20$\times$ and 100$\times$, and transient heating under 100$\times$ to get the temperature rise in each heating scenario.

The last input needed to solve the heat conduction model is the solid cross-sectional area A_c of the bundle, which we determine by utilizing the radial breathing modes (RBM) of SWCNTs. The RBM are known to be size-dependent and are frequently used to estimate the diameter of individual SWCNTs within the bundle. The frequency of the RBM excitations (ω_{RBM}) is inversely proportional to the tube diameter (d) as $d = 223.75/\omega_{RBM}$. In this study, the RBM peaks are acquired for each

location and are used to determine the diameters of individual SWCNTs to resolve the internal structure. To account for the peaks, any abrupt discontinuity in the Raman spectrum is considered to represent a distinct peak [20], which aligns with the multiple peak fitting in Fig. 4. The frequency-diameter relationship described earlier allows us to calculate the diameter of each unique SWCNT based on the frequency of each distinct peak. The bundle's total solid area is then calculated as $A_c = \sum (\pi/4)\left(d_o{}^2 - d_i{}^2\right)$, where d_o is the diameter of individual SWCNTs, $d_i = d_o - 2t$, and $t = 0.335$ nm as the SWCNT wall thickness. The summation is over the different RBM distinct peaks, each corresponding to one unique SWCNT with a diameter calculated based on the frequency-diameter relationship. We acknowledge that the number of individual SWCNTs per RBM peak could vary. In other words, having more than one SWCNT with the same diameter is possible. However, the number of distinct peaks observed indeed suffices to populate 75 % of the nominal size of the bundle, as observed under the AFM. This leaves very little room for more than one individual SWCNT per RBM peak. Similar treatment has been carried out in our previous works where the uncertainty was projected on the inferred ITR. A more detailed discussion of the method can be found in our recently published work [20]. Looking at Eq. (1), one can notice that this uncertainty mainly affects the measured ITR but will not impact κ since the composite term $R'\cdot A_c$ is invariant and overestimating one parameter will underestimate the other.

The RBM peaks shown in Fig. 4 for the four different locations exhibit a variation in the frequency and their number, which aligns with the variation in the bundle's height as observed under the AFM. These locations are roughly separated by 2–3 μm along the bundles' length direction. The solid areas calculated using the previous equations are summarized in Table 2. The monotonic reduction in the size of the bundle along the four locations is explained by the aligning procedure during which the bundle is pushed against the substrate, which ensures the alignment of the SWCNT with the direction of the applied force and causes a reduction in their diameters along the pressing motion as described earlier. Hence, based on the above observation, we conclude
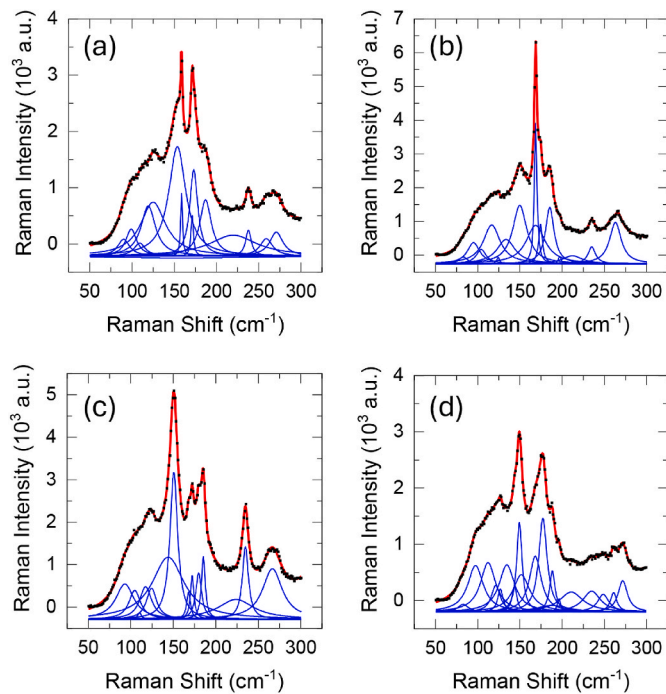

Fig. 4. The radial breathing modes (RBM) of the SWCNT bundle are shown for (a) Location #1, (b) Location #2, (c) Location #3, and (d) Location #4. The multiple peak fitting (MPF) is performed using the Lorentzian function. (A colour version of this figure can be viewed online.)

that the brushing direction during the alignment process took place from location 4, which has the largest size, towards location 1, which has the smallest one. This is confirmed by optical observation of the whole sample pattern caused by brushing. Note the RBM can only reveal the tubes exhibiting an electronic transition E_{ii} that matches the incident laser energy, as observed in the well-known Kataura plot [25]. As explained earlier, we have checked our SWCNT tube numbers and their occupied space against the AFM measurement results and confirmed the fitted RBM peaks populate the bundle and leave very little room to populate more tubes. The utilization of the RBM to characterize the entire bundle makes a sound approach, and it has been used earlier in the literature due to the extreme difficulty in resolving the internal structure of the bundle [12,15,20].

After calculating the solid area, we solve the heat conduction equation to get the local temperature rise as a function of κ and ITR. Since the experimental normalized RSC ($\Theta_{exp} = \psi_{FR}/\psi_{CW}$) represents the average relative temperature rise over the laser heating area, we shall average the theoretical results accordingly [12]. For steady-state heating, the Raman-intensity weighted average temperature rise can be calculated by integrating over the spatial domain as $\Delta \overline{T}_{CW} = \int_0^{x_0} I\Delta T\cdot dx / \int_0^{x_0} I\cdot dx$. Since the temperature is time-dependent for transient state heating, the temperature rise must be weighted over both temporal and spatial domains as $\Delta \overline{T}_{tr} = \int_0^{t_0}\int_0^{x_0} I\Delta T\cdot dxdt / \int_0^{t_0}\int_0^{x_0} I\cdot dxdt$, where t_0 is the laser heating time (200 ns). In both cases, I is the intensity taken as $I = I_0 \exp\left(-x^2/r_0^2\right)$.

4. Results and discussion

4.1. Interfacial thermal resistance and thermal conductivity

The weighted theoretical temperature rise ratio $\Theta_{th} = \Delta \overline{T}_{tr}/\Delta \overline{T}_{CW}$, which stems from the heat conduction solution, can then be plotted as a function of both the ITR and κ for the two scenarios $\Theta_{20\times}$ and $\Theta_{100\times}$, each of which compares the transient state thermal response under $100\times$ to the steady state one under the $20\times$ and $100\times$, respectively. One can notice the different outputs for the theoretical results under different objective lenses, as shown in the contours in Fig. 5a–b. This, in fact, is a manifestation of the unique contribution of the ITR and κ as established earlier in Section 2.2. For each location, the experimentally measured values for the relative average temperature rise (Θ_{exp}) are mapped to both contours (a and b), shown as dashed lines in Fig. 5a–b. The dashed line solutions are then combined to pinpoint κ and ITR values. The two lines in Fig. 5c describe the coupled relationship between the ITR and κ on thermal transport under the two different laser spot sizes, where the intersection is the solution that satisfies the heat equation under the two heating scenarios. The results for the second location are shown on the graph where κ is measured to be 246 W m^{-1} K^{-1}, whereas the ITR is found to be 990 K m W^{-1}.

The solutions shown in Fig. 5c are obtained by mapping out the measured values of Θ_{exp}, which carry their uncertainty as shown in Fig. 3f. To account for that, the experimental normalized RSC are assumed to follow a Gaussian distribution around their measured values that take the form of $\Omega_i = \exp\left[-\left(\Theta_i - \Theta_{exp,i}\right)^2/2\sigma_i{}^2\right]$ [23] where Ω is the probability distribution function, $\Theta_{exp,i}$ is the experimental normalized RSC, Θ_i is the theoretical normalized RSC, σ_i is the experimental uncertainty in RSC. The index i refers to calculating the probability distribution function for either $100\times$ or $20\times$ objective lens as illustrated in Fig. 5d–e, respectively, for Location #2. The final uncertainty is found by computing the composite probability distribution function $\Omega_{Total} = \Omega_{20\times}\cdot\Omega_{100\times}$ as shown in Fig. 5f. The results for κ and ITR measurements for different locations are shown in Fig. 5g, where we plot them against the solid area of each location as calculated in Table 1. The error bars correspond to the composite probability distribution function Ω_{Total} greater than 0.7. We find that the ITR results range between 975 and 1200 K m W^{-1} with some correlation between the ITR and solid area of
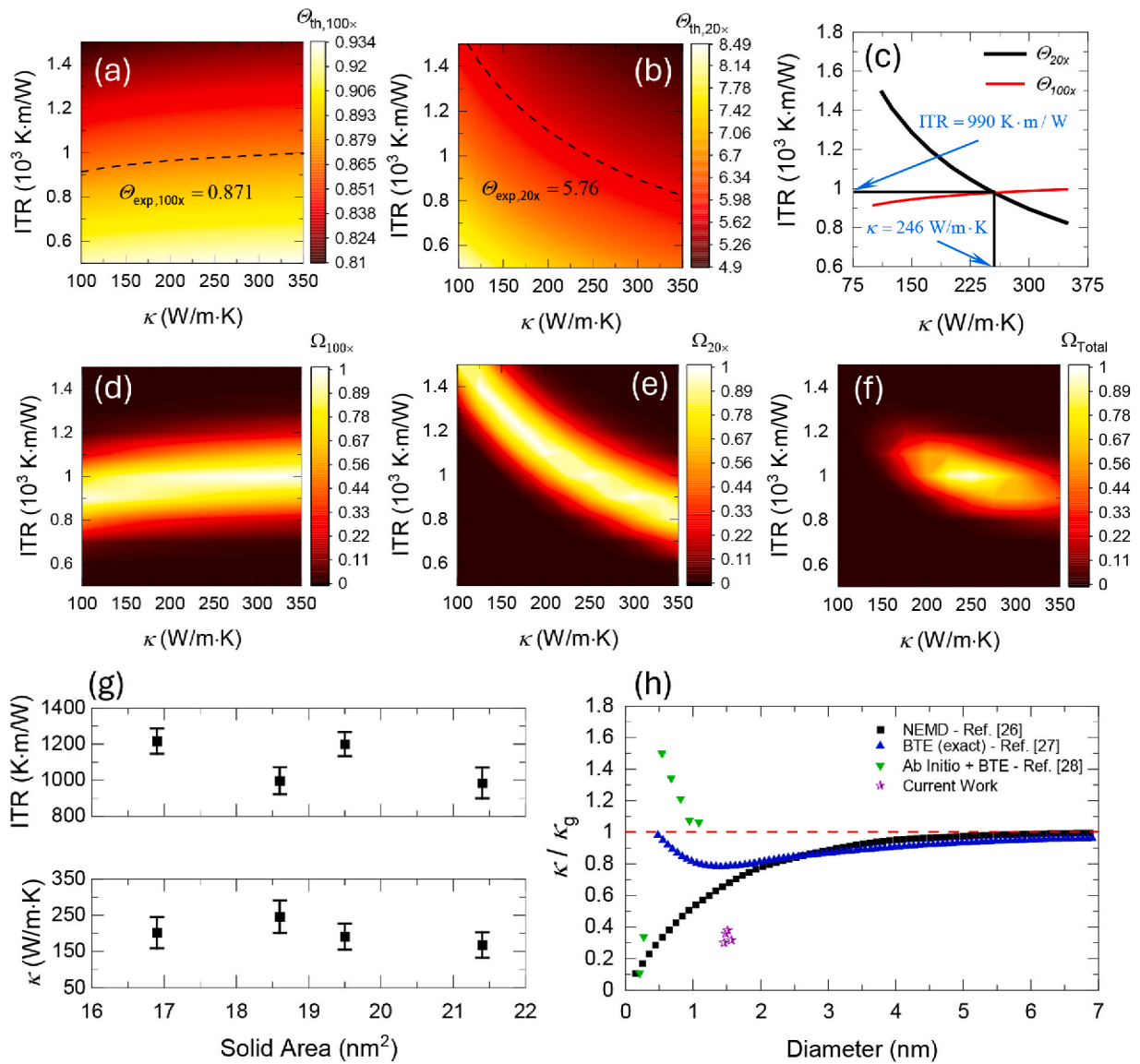
Fig. 5. The theoretical average temperature rise ratio (Θ_{th}) as a function of ITR and κ for Location #2 under (a) 100× and (b) 20× objective lens. The dashed lines represent the experimental result (Θ_{exp}) as measured. (c) The intersection of the experimental results represents the solution for the heat conduction model to determine κ and ITR for Location #2. The normalized probability distribution function $\Omega(\kappa, ITR)$ for (d) $\Theta_{100\times}$ (e) $\Theta_{20\times}$. (f) The composite probability distribution function corresponds to the uncertainty of the simultaneous measurement for κ and ITR. (g) The measured κ and ITR as a function of the solid area for the four different locations where error bars correspond to values Ω_{Total} larger than 0.7. (h) The κ of SWCNT normalized to that of graphene (κ_g) as a function of its diameter for our sample, compared with results from the literature. The dashed pink line corresponds to the unity ratio. (For interpretation of the references to colour in this figure legend, the reader is referred to the Web version of this article.)

the SWCNT bundle. Generally, a larger solid area corresponds to a larger contact between the sample and the substrate, enhancing energy transport and yielding lower thermal resistance. As for κ, it varies between 180 and 246 W m^{-1} K^{-1} and shows almost no clear dependency on the calculated solid area, which we attempt to elaborate on its size dependency in the following section.

The reported results for the ITR are consistent with previous measurements done in our lab using the energy transport state-resolved Raman (ET-Raman), where it takes an intermediate value between the previously reported ones: 1670–3010 [12] and 530–725 [20] K m W^{-1}. The first of the two previous studies suggests loose contact between the bundle and the substrate through a qualitative model explaining the order of magnitude difference. We note that the κ in the former studies has been borrowed from a previous measurement [13] for suspended SWCNT to be 50 W m^{-1} K^{-1}, which is 3–4 times lower than the currently measured ones. The discrepancies are believed to have stemmed from

the different experimental setups, the size difference, and the defect level within each sample. Nevertheless, we find that the reported results fit seamlessly within the range of reported values found in the literature, which spans several orders of magnitude: 10–10^4 W m^{-1} K^{-1}. To show the significance of a simultaneous measurement, we process the current data and solve the heat conduction model for Location #2 while using the pre-measured κ (50 W m^{-1} K^{-1}). The results yield an ITR of 780 K m W^{-1} whereas the actual measured one based on the simultaneous measurement approach is 990 K m W^{-1}. For the same temperature rise, overestimating one (e.g., the conduction resistance) will underestimate the other (the ITR in this case) and vice versa. Hence, we believe the current study significantly advances the accuracy of thermal characterization techniques for low-dimensional materials, where the common assumption of neglecting the ITR or relying on pre-measured data is eliminated. The proposed technique yields a highly reliable measurement for ITR and κ when compared to previous work found in literature,

with the advantage of being measured simultaneously for the exact location, eliminating the uncertainty associated with borrowing a pre-measured value for κ. The results shown in Fig. 5g suggest a narrower confidence region for the ITR compared to κ, meaning that the uncertainty associated with the ITR is lower than that of the reported κ.

4.2. Size-dependent thermal conductivity of SWCNT

The size effect on the κ of SWCNTs has been studied widely in the literature where diverse insights are inferred, as illustrated in Fig. 5h. Cao and Qu [26] utilized non-equilibrium molecular dynamics (NEMD) simulations to study SWCNTs with lengths up to micrometers. They observe that κ increases with tube diameter, eventually approaching κ of graphene. This trend is attributed to enhanced participation of low and moderate-frequency radial breathing modes in larger diameter tubes. Lindsay et al. [27] employed an exact numerical solution to the phonon Boltzmann transport equation (BTE), including contributions from optical phonon modes, to explore κ of SWCNTs and their convergence to the graphene limit. The results revealed a non-monotonic diameter dependence of κ, with a minimum at modest diameters (~1.5 nm). The lower phonon-phonon scattering rate explains the convergence to graphene's κ for very small diameters due to a smaller number of activated phonon modes since the energy gap between optical and acoustic phonons is higher for smaller diameter SWCNT as supported by several studies in literatures.

Yue et al. [28] conducted a first-principles study combining anharmonic lattice dynamics with BTE calculations to elucidate the diameter dependence of κ in SWCNTs. They found that κ increases as the diameter decreases within the 4.07 to 10.85 Å, exceeding the in-plane κ of graphene in this range. Their study highlighted that ultra-thin SWCNTs have lower thermal conductivities, consistent with previous MD simulations, and attributed the decreasing κ with increased diameter to the increased optical phonon participation in scattering processes. Zhu and Li [29] used MD simulations to investigate the κ of ultrathin SWCNTs, specifically (2, 1) CNTs, which exhibited significantly lower κ compared to larger diameter CNTs like (2, 2) and (5, 5). They attributed this reduction to the softening of acoustic phonon modes, resulting in decreased phonon group velocities and lifetimes.

One can see that the previous studies offer diverse and somewhat inconsistent conclusions about the size effect, even for individual SWCNTs. For a bundle, the underlying physics becomes even more complicated where the interactions between different tubes are to be taken into consideration, and κ can be as low as 50–200 W m^{-1} K^{-1} as delineated in previous work [13,30] which are in line with the reported one in this study. In general, κ of a SWCNT bundle is 1–2 orders of magnitude lower than individual SWCNT [3,31]. It is worth noting that the thermal conductivity of graphene (κ_g) used for normalization in Fig. 5h is taken as 2436 and 3409 W m^{-1} K^{-1} for Ref. [27] and Ref. [28], respectively. For Ref. [26], however, κ_g values varied between 500 and 2500 W m^{-1} K^{-1}, where the length of the graphene sheet heavily influences the values. Nevertheless, all CNTs κ are normalized with the value of κ_g of the same length.

For supported graphene on SiO$_2$, Seol et al. [32] reported κ_g to be around 600 W m^{-1} K^{-1} at room temperature, significantly lower than suspended graphene. The authors explain this reduction by phonon leaking through the interface and significant interface scattering of flexural phonon modes, which normally contribute substantially to κ_g in suspended graphene. To scale our measurements of κ with that of supported graphene, we first find the average diameter of individual SWCNTs within the bundle for each location. To calculate this, we find the average solid area $\widetilde{A}_c = A_c/N$, where A_c is the total solid area and N is the number of SWCNTs as observed under the RBM both are listed in Table 2. We then calculate the average diameter by solving for $\widetilde{d}$ from the following equation: $\widetilde{A}_c = (\pi/4)\left(\widetilde{d}^2 - (\widetilde{d} - 2t)^2\right)$, where t is the thickness of SWCNT wall as described earlier in Section 3. The average

SWCNT diameter of locations 1 through 4 is calculated to be 1.48, 1.51, 1.57, 1.46 nm, respectively, as summarized in Table 2. The measured values of κ in the current study are scaled to that of SiO$_2$-supported graphene and are shown in Fig. 5h. The κ of the bundle relative to κ_g is around 33 % for the different studied locations. This significant reduction is caused by structural defects of individual nanotubes and the substrate interaction described above. The structural defect has been studied in our recent work for suspended SWCNT bundles [13] by evaluating the residual thermal reffusivity. This residual value is tightly related to phonon scattering due to structural defects at the limit of 0 K temperature when Umklapp scattering is negligible due to the low phonon population. A more in-depth discussion of the method can be found in Ref. [13]. The average thermal domain sizes for two SWCNT bundles are 46.0 nm and 61.9 nm, respectively.

The structural deformation of SWCNTs, the interfacial states between different tubes, and defects on the SWCNT surfaces significantly affect the measured κ. The curly nature of the SWCNT bundles means that the heat transfer path is longer than the assumed linear path within the heat conduction model, leading to reduced κ. Structural deformations such as bending and twisting disrupt the continuity of phonon transport channels by introducing additional scattering sites and altering phonon dispersion relations. These inter-tube interactions act as barriers to phonon transport, ultimately impacting the bundles' overall κ. While these mechanisms are very challenging to disentangle experimentally, a computational study by Shigo et al. [4] shows that low-frequency phonons, the primary heat carriers, are more susceptible to inter-tube interactions, and the reduction in κ is found to scale with the length of the bundle. The bundling effect is experimentally shown to reduce κ by two orders of magnitude for bundles with more than 13 individual tubes inside, where it was measured to be around 200 W m^{-1} K^{-1} [3], consistent with the measured values in the current study for ~15 tubes. We further attempt to disentangle the unique contribution of each SWCNT within the bundle to the measured κ to elaborate on the results shown in Fig. 5g. However, we find that the change in κ at different locations is very minute and is of the order of the uncertainty associated with the measurement. Hence, no clear size dependence can be rigorously inferred from the measured values.

5. Conclusion

In this work, using the FET-Raman technique, we reported the first-time simultaneous characterization of the κ and ITR of a SWCNT bundle (less than 10 nm thickness) supported by a SiO$_2$ substrate. Such measurement is nearly impossible using the conventional steady-state Raman technique as the laser absorption in the sample cannot be obtained due to the remarkable complexity of the SWCNT bundle's structure. The distinction between the in-plane and cross-plane thermal transport was accomplished by using multiple laser heating sizes and distinct energy transport states, each of which carries a unique contribution from the ITR and κ. The thermal response to different heating scenarios was recorded for four locations in the sample and used to numerically extract the ITR and κ from solving the heat conduction equation. The height of the bundle was measured to vary from 6 to 10 nm, where individual SWCNTs have a distribution of diameters that ranges from 0.8 to 2.7 nm as per the RBM analysis, with an average diameter of ~1.5 nm. The reported values for ITR and κ varied from 975 to 1200 K m W^{-1} and 180–246 W m^{-1} K^{-1}, respectively. The ITR is found to be very comparable to a recent measurement done in our lab for supported SWCNT/SiO$_2$. Furthermore, the ITR showed an overall decreasing trend as bundle size increases, confirming that the contact area between the bundle and the substrate plays a significant role in determining the local energy transport, whereas no clear size dependence can be inferred from the reported data for κ. The κ of the supported SWCNT is compared with that of supported graphene κ_g on a SiO$_2$ substrate where the ratio κ/κ_g is found to be about 33 %. We attribute the reduction in κ to the structural defects in the samples reported earlier for

suspended SWCNTs, which have been fabricated and transferred in similar circumstances, and to the bundling effect. This work provides some of the most advanced understanding of energy transport in supported SWCNTs, and the FET-Raman-based metrology can be readily applied to other supported 1D nanoscale materials for κ and ITR measurement.

CRediT authorship contribution statement

Ibrahim Al Keyyam: Writing – original draft, Visualization, Investigation, Formal analysis, Data curation. **Baini Li:** Writing – review & editing, Resources, Methodology, Investigation. **Tianyu Wang:** Writing – review & editing, Supervision, Resources, Project administration, Methodology, Investigation, Funding acquisition, Formal analysis, Data curation, Conceptualization. **Cheng Deng:** Writing – review & editing, Resources, Project administration, Methodology, Investigation, Funding acquisition, Formal analysis, Data curation, Conceptualization. **Xinwei Wang:** Writing – review & editing, Supervision, Software, Resources, Project administration, Methodology, Investigation, Funding acquisition, Formal analysis, Conceptualization.

Declaration of competing interest

The authors declare the following financial interests/personal relationships which may be considered as potential competing interests: Cheng Deng reports financial support was provided by National Natural Science Foundation of China. Cheng Deng reports a relationship with Guangdong Basic and Applied Basic Research Foundation that includes: funding grants. If there are other authors, they declare that they have no known competing financial interests or personal relationships that could have appeared to influence the work reported in this paper.

Acknowledgements

References

[1] X. Guo, S. Cheng, W. Cai, Y. Zhang, X.-a. Zhang, A review of carbon-based thermal interface materials: mechanism, thermal measurements and thermal properties, Mater. Des. 209 (2021) 109936.
[2] Y. Feng, Y. Sato, T. Inoue, M. Liu, S. Chiashi, R. Xiang, K. Suenaga, S. Maruyama, Drastically reduced thermal conductivity of self-bundled single-walled carbon nanotube, Carbon 201 (2023) 433–438.
[3] Y. Feng, T. Inoue, H. An, R. Xiang, S. Chiashi, S. Maruyama, Quantitative study of bundle size effect on thermal conductivity of single-walled carbon nanotubes, Appl. Phys. Lett. 112 (19) (2018) 191904.
[4] T. Shiga, Y. Terada, S. Chiashi, T. Kodama, Effect of bundling on phonon transport in single-walled carbon nanotubes, Carbon (2024) 119048.
[5] B. Kumanek, D. Janas, Thermal conductivity of carbon nanotube networks: a review, J. Mater. Sci. 54 (10) (2019) 7397–7427.
[6] B. Goh, K.J. Kim, C.-L. Park, E.S. Kim, S.H. Kim, J. Choi, In-plane thermal conductivity of multi-walled carbon nanotube yarns under mechanical loading, Carbon 184 (2021) 452–462.
[7] A.E. Aliev, M.H. Lima, E.M. Silverman, R.H. Baughman, Thermal conductivity of multi-walled carbon nanotube sheets: radiation losses and quenching of phonon modes, Nanotechnology 21 (3) (2010) 035709.
[8] K. Chawla, J. Cai, D. Thompson, R. Thevamaran, Superior thermal transport properties of vertically aligned carbon nanotubes tailored through mesoscale architectures, Carbon 216 (2024) 118526.
[9] J. Yang, S. Waltermire, Y. Chen, A.A. Zinn, T.T. Xu, D. Li, Contact thermal resistance between individual multiwall carbon nanotubes, Appl. Phys. Lett. 96 (2) (2010) 023109.
[10] H. Maune, H.-Y. Chiu, M. Bockrath, Thermal resistance of the nanoscale constrictions between carbon nanotubes and solid substrates, Appl. Phys. Lett. 89 (1) (2006) 013109.
[11] L. Shi, J. Zhou, P. Kim, A. Bachtold, A. Majumdar, P.L. McEuen, Thermal probing of energy dissipation in current-carrying carbon nanotubes, J. Appl. Phys. 105 (10) (2009) 104306.
[12] I. Al Keyyam, M. Rahbar, E. Shi, B. Li, T. Wang, X. Wang, Thermal conductance between <6 nm single-walled carbon nanotube bundle and Si substrate, J. Phys. Chem. C 128 (3) (2024) 1505–1517.
[13] M. Rahbar, B. Li, N. Hunter, I. Al Keyyam, T. Wang, E. Shi, X. Wang, Observing grain boundary-induced phonons mean free path in highly aligned SWCNT bundles by low-momentum phonon scattering, Cell Reports Physical Science (2023) 101688.
[14] J. Liu, I. Al Keyyam, Y. Xie, X. Wang, Perspectives on interfacial thermal resistance of 2D materials: Raman characterization and underlying physics, Surface Science and Technology 2 (1) (2024) 8.
[15] Y. Feng, Y. Sato, T. Inoue, R. Xiang, K. Suenaga, S. Maruyama, Enhanced thermal conductivity of single-walled carbon nanotube with axial tensile strain enabled by boron nitride nanotube anchoring, Small 20 (16) (2024) 2308571.
[16] T.-Y. Choi, D. Poulikakos, J. Tharian, U. Sennhauser, Measurement of the thermal conductivity of individual carbon nanotubes by the four-point three-ω method, Nano Lett. 6 (8) (2006) 1589–1593.
[17] J.R. Lukes, H. Zhong, Thermal conductivity of individual single-wall carbon nanotubes, J. Heat Tran. 129 (6) (2006) 705–716.
[18] E. Shi, H. Li, L. Yang, J. Hou, Y. Li, L. Li, A. Cao, Y. Fang, Carbon nanotube network embroidered graphene films for monolithic all-carbon electronics, Adv. Mater. 27 (4) (2015) 682–688.
[19] N. Hunter, N. Azam, H. Zobeiri, R. Wang, M. Mahjouri-Samani, X. Wang, Interfacial thermal conductance between monolayer WSe₂ and SiO₂ under consideration of radiative electron–hole recombination, ACS Appl. Mater. Interfaces 12 (45) (2020) 51069–51081.
[20] I. Al Keyyam, M. Rahbar, N. Hunter, B. Li, T. Wang, E. Shi, X. Wang, T^{-n} (n: 2.4~2.56) temperature dependence of thermal resistance at single-walled carbon nanotubes/SiO₂ interface at <8 nm scale, Int. J. Heat Mass Tran. 226 (2024) 125513.
[21] W. Zhu, G. Zheng, S. Cao, H. He, Thermal conductivity of amorphous SiO₂ thin film: a molecular dynamics study, Sci. Rep. 8 (1) (2018) 10537.
[22] R. Wang, T. Wang, H. Zobeiri, P. Yuan, C. Deng, Y. Yue, S. Xu, X. Wang, Measurement of the thermal conductivities of suspended MoS₂ and MoSe₂ by nanosecond ET-Raman without temperature calibration and laser absorption evaluation, Nanoscale 10 (48) (2018) 23087–23102.
[23] P. Yuan, J. Liu, R. Wang, X. Wang, The hot carrier diffusion coefficient of sub-10 nm virgin MoS₂: uncovered by non-contact optical probing, Nanoscale 9 (20) (2017) 6808–6820.
[24] R. Prasher, Predicting the thermal resistance of nanosized constrictions, Nano Lett. 5 (11) (2005) 2155–2159.
[25] C.-Y. Liu, J.-Y. Hsiao, E.Y. Li, A global prediction of the Kataura plot for chiral carbon nanotubes: topological family effect revealed in the natural helical crystal lattice scheme, Carbon 208 (2023) 72–81.
[26] A. Cao, J. Qu, Size dependent thermal conductivity of single-walled carbon nanotubes, J. Appl. Phys. 112 (1) (2012) 013503.
[27] L. Lindsay, D.A. Broido, N. Mingo, Diameter dependence of carbon nanotube thermal conductivity and extension to the graphene limit, Phys. Rev. B 82 (16) (2010) 161402.
[28] S.-Y. Yue, T. Ouyang, M. Hu, Diameter dependence of lattice thermal conductivity of single-walled carbon nanotubes: study from ab initio, Sci. Rep. 5 (1) (2015) 15440.
[29] L. Zhu, B. Li, Low thermal conductivity in ultrathin carbon nanotube (2, 1), Sci. Rep. 4 (1) (2014) 4917.
[30] J. Hone, M.C. Llaguno, M.J. Biercuk, A.T. Johnson, B. Batlogg, Z. Benes, J. E. Fischer, Thermal properties of carbon nanotubes and nanotube-based materials, Appl. Phys. Mater. Sci. Process 74 (3) (2002) 339–343.
[31] C. Yu, L. Shi, Z. Yao, D. Li, A. Majumdar, Thermal conductance and thermopower of an individual single-wall carbon nanotube, Nano Lett. 5 (9) (2005) 1842–1846.
[32] J.H. Seol, I. Jo, A.L. Moore, L. Lindsay, Z.H. Aitken, M.T. Pettes, X. Li, Z. Yao, R. Huang, D. Broido, N. Mingo, R.S. Ruoff, L. Shi, Two-dimensional phonon transport in supported graphene, Science 328 (5975) (2010) 213–216.